Journal Pre-proof

Electronic transport, ionic activation energy and trapping phenomena in a polymer-hybrid halide perovskite composite

Mauro Leoncini, Roberto Giannuzzi, Antonella Giuri, Silvia Colella, Andrea Listorti, Vincenzo Maiorano, Aurora Rizzo, Giuseppe Gigli, Salvatore Gambino

PII: S2468-2179(21)00057-5

DOI: https://doi.org/10.1016/j.jsamd.2021.07.006

Reference: JSAMD 383

To appear in: *Journal of Science: Advanced Materials and Devices*

Received Date: 7 March 2021

Revised Date: 14 July 2021

Accepted Date: 20 July 2021

Please cite this article as: M. Leoncini, R. Giannuzzi, A. Giuri, S. Colella, A. Listorti, V. Maiorano, A. Rizzo, G. Gigli, S. Gambino, Electronic transport, ionic activation energy and trapping phenomena in a polymer-hybrid halide perovskite composite, *Journal of Science: Advanced Materials and Devices*, https://doi.org/10.1016/j.jsamd.2021.07.006.

Electronic transport, ionic activation energy and trapping phenomena in a polymer-hybrid halide perovskite composite

Mauro Leoncini[1,2], Roberto Giannuzzi[1,2], Antonella Giuri[1], Silvia Colella[3], Andrea Listorti[4], Vincenzo Maiorano[1], Aurora Rizzo[1], Giuseppe Gigli[1,2], Salvatore Gambino[1,*]

1 CNR NANOTEC – Istituto di Nanotecnologia, c/o Campus Ecotekne, Via Monteroni, 73100 Lecce, Italy
2 Dipartimento di Matematica e Fisica "E. De Giorgi", Università del Salento, Campus Ecotekne, via Arnesano, 73100 Lecce, Italy
3 CNR NANOTEC - c/o Dipartimento di Chimica, Università di Bari, Via Orabona 4, 70126 Bari, Italy
4 Dipartimento di Chimica, Università di Bari, Via Orabona 4, 70126 Bari, Italy

*Corresponding author. Email: salvatore.gambino@nanotec.cnr.it

Acknowledgments

The authors gratefully thank Sonia Carallo for technical support and Barbara Cortese for editing the English of this manuscript. This research was funded by Ministry of University and Scientific Research (MIUR), project FISR—C.N.R. "Tecnopolo di nanotecnologia e fotonica per la medicina di precisione", grant number: CUP B83B17000010001.

Electronic transport, ionic activation energy, and trapping phenomena in a polymer-hybrid halide perovskite composite

Abstract

The exploitation of methylammonium lead iodide perovskite-polymer composites is a promising strategy for the preparation of photoactive thin layers for solar cells. The preparation of these composites is a simple fabrication method with improved moisture stability when compared to that of pristine perovskite films. To deepen the understanding of the charge transport properties of these films, we investigated charge carrier mobility, traps, and ion migration. For this purpose, we applied a combinatory measurement approach that proves how such composites can still retain an ambipolar charge transport nature and the same mobility values of the related perovskite. Furthermore, thermally stimulated current measurements revealed that the polymer influenced the creation of additional defects during film formation without affecting charge mobility. Finally, impedance spectroscopy measurements suggested the addition of starch may hinder ion migration, which would require larger activation energies to move ions in composite films. These results pave the way for new strategies of polymer-assisted perovskite film development.

1. Introduction

Hybrid (organic-inorganic) perovskite semiconductors are currently among the most promising candidates for the development of alternative solar cells. In less than ten years, perovskite solar cells (PSCs) have reached a power conversion efficiency (PCE) of 25.5% [1]. Despite this remarkable achievement in device efficiency, which makes PSCs already suitable for the market, properties like straightforward processing and operative device stability are often below the standard to be technologically scaled up. For example, top-performing PSCs are realized by solution cast techniques like ink-jet, slot die, spray coating, or roll-to-roll methods [2], all of which require a “timely” anti-solvent dripping that is hardly suitable for large scale production.

Over the last few years, the use of polymers as templating agents for the growth of hybrid perovskite materials has emerged as an efficient strategy to confer improved stability and processability to the active layer [3],[4],[5]. In particular, our group has developed a

methylammonium lead iodide ($MAPbI_3$) perovskite-starch composite (so-called MAPI-composite), which has been used as a light harvester for solar cells [3],[6] and light-emitting devices [7]. These devices are characterized by a simple fabrication process and result in improved device stability while maintaining similar performance compared to that of pristine perovskite-based devices. In order to understand the limits and advantages of these composites, it is important to investigate their charge transport mechanism as it is strictly related to device efficiency. The composite we propose in this research consists of an active (perovskite) and a passive (starch) component, the latter of which has been demonstrated to be beneficial for i) the formation of perovskites via a single-step polymer-assisted anti-solvent free process, ii) film stability, and iii) mechanical stress [3]. However, with the composite being an insulator, it does not play any active role in electronic charge transport. Furthermore, in a composite, defect states arising from boundaries between the perovskite and polymer may introduce traps and recombination centres that would have a direct influence on the transport mechanism of the charge carriers and thus on device efficiency. Other solution-processable materials like organic semiconductors have demonstrated that carrier mobility depends on a wide range of factors such as the materials' chemical structure, molecular weight, processing conditions (solvents, casting technique), and environmental conditions [8]. Furthermore, in perovskites, the study of the electronic charge transport mechanism is even more complex because it is also influenced by ionic conduction. Thus, mixed ionic and electronic charge transport must be considered [9],[10],[11].

To better address this challenge, we combine space charge limited current (SCLC) measurements with other methods of investigation, such as thermally stimulated current (TSC) and impedance spectroscopy (IS), to access to the main parameters governing the charge transport of the proposed MAPI-composite. By combining these different techniques, we disentangle the dependence of electronic transport from ionic transport and reveal electronic (mobility and trapping phenomena) and ionic (activation energies) charge transport dynamics. We demonstrate that the MAPI-composite still retains ambipolar charge transport nature and the same mobility values of the perovskite. This is the first time that the electro-optical properties of such a MAPI-composite have been studied. Moreover, we were also able to correlate these properties to solar cells performance and film morphology.

2. Materials and Methods

2.1 Materials

Ultra-dry 99.999% lead (II) iodide (PbI_2) (metal basis) was purchased from Alfa Aesar; methylammonium iodide (MAI) was obtained from Greatcell Solar; corn starch (Maizena) was supplied from Sigma-Aldrich; PEDOT:Complex (PEDOT:Cx) (HTL Solar 3) was supplied from Heraeus; poly[N,N0-bis(4-butylphenyl)-N,N0-bis(phenyl) benzidine] (poly-TPD) from Solaris Chem Inc.; [6,6]-phenyl C_{61} butyric acid methyl ester (PCBM) was purchased from Nano-c. All the materials were used as received without further purification. Solution preparation and device realization are reported in the appendix.

2.2 Realization of MAPI and MAPI-composite thin films

MAPI thin films were realized via a standard one-step procedure inside an N_2 filled glove-box. First, perovskite precursors in DMF/DMSO solution were spin cast at 4000 rpm for 25 s, during which a "timely" (after 10 s) anti-solvent of 200 µl toluene was dropped on top. Subsequently, the spin-coated film was annealed onto a hot plate at 100°C for 10 min (Fig. 1, top). Meanwhile, the MAPI-composite thin film was realized via a one-step polymer-assisted anti-solvent free procedure. The MAPI-composite solution in DMSO was spin cast at 9000 rpm for 20 s and then directly annealed on a hot plate at 100°C for 30 min (Fig. 1, bottom).

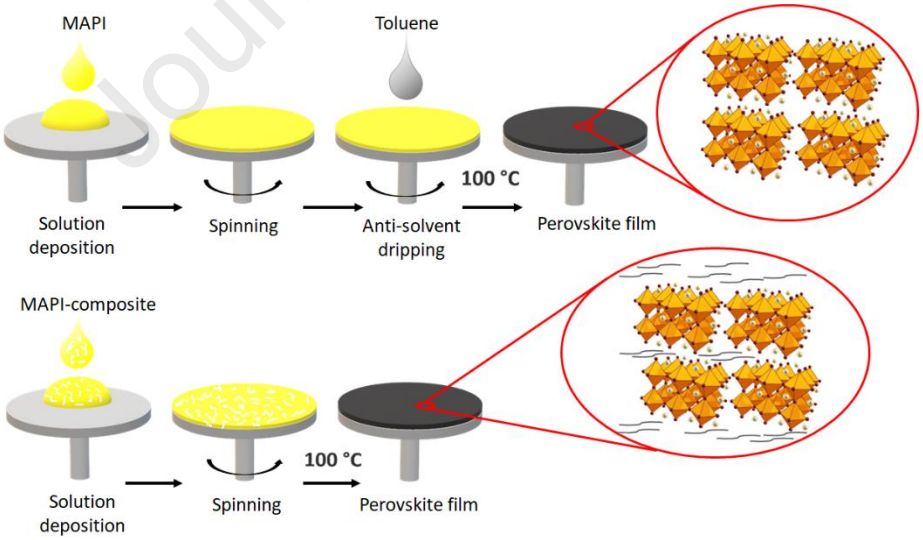

Figure 1. Schematic illustration of the standard one-step (top) and one-step anti-solvent free (bottom) deposition method of MAPI and MAPI-composite thin films.

2.3 XRD and SEM thin films characterization

X-ray diffraction (XRD) spectra of the perovskite films were acquired at room temperature by a PANanalytical X'Pert-PRO MRD diffractometer equipped with a Cu Kα source (λ = 1.5405 Å). The scanning electron microscopy (SEM) images were collected with Carl Zeiss Auriga40 Crossbeam (Zeiss) instrument in high vacuum and high-resolution mode at 5 kV acceleration voltage and was equipped with Gemini column and an integrated high efficiency in-lens detector.

2.4 SCLC measurements

SCLC measurements were performed in the dark and the sample was loaded into a cryostat under low dynamic vacuum (10^{-2} mbar). Current-voltage characteristics were recorded using a computer controlled pico-ammeter (HP 4140B).

2.5 TSC measurements

TSC measurements were performed by loading the sample into a sample stage (Linkam LTS420E-P) and maintaining it under dynamic vacuum. The temperature was allowed to vary between 77 K and 300 K. Trap filling was achieved by illuminating the sample via a halogen lamp for 5 min at 160 K. After a dwell time of 15 min at 160 K without light, the temperature was increased at a constant rate of 5 K/min. Thermally stimulated currents were recorded using a computer controlled pico-ammeter (HP 4140B) without applying an external bias to the device.

2.6 IS measurements

Impedance spectroscopy was carried out at different temperatures by loading the sample into a sample stage (Linkam LTS420E-P) under illumination using a white LED. IS measurements were performed at short-circuit with a 20 mV perturbation in the 10^{6} to 10^{-2} Hz range using an Autolab/PGSTAT302N (Eco-Chemie, The Netherlands) operating in two-electrode mode. NOVA 1.11 software was used to generate data. Z-view equivalent circuit modelling software (Scribner) was used to fit the spectra.

3. Results and Discussion

3.1 Perovskite solar cells

Perovskite solar cells based on MAPI and MAPI-composite films were realized in a p-i-n configuration as shown in Fig. 2a (inset), which is also where the current-density-voltage (J-V) characteristics are shown. The main PSC parameters, together with statistical data (average values) estimated for more than ten devices realized and characterized under the same experimental

conditions, are reported in Table 1. It is clear that MAPI and MAPI-composite based PSCs exhibit similar performances both in terms of power conversion efficiency (PCE ≈ 17-18 %) as well as fill factor (FF ≈ 76-78 %), short-circuit current (J_{sc} ≈ 20-21 mA/cm^2), and V_{oc} ≈ 1.1 V. The incident photon to current conversion efficiency (IPCE) spectra of both the MAPI and MAPI-composite based solar cells are shown Fig. 2b, which are consistent with both MAPI and MAPI-composite thin film absorption spectra reported in Fig. S1. The integrated photocurrent densities are 20.8 and 19.2 mA/cm^2 for PSCs with MAPI and MAPI-composite, respectively, which are in good agreement with J_{sc} determined from the J−V curves. A complete study on MAPI-composite optimization has been reported elsewhere [3].

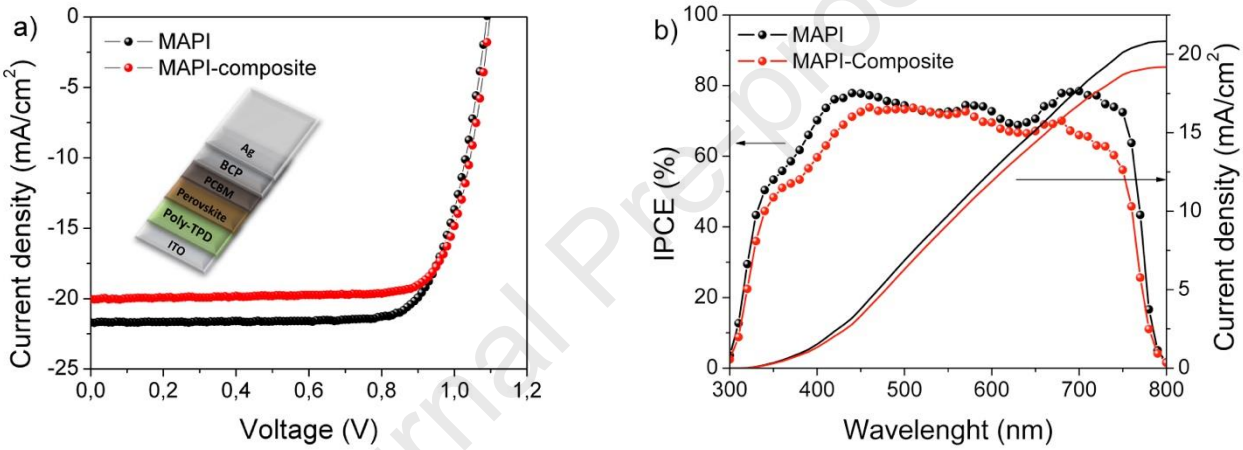

Figure 2. Best samples of the MAPI and MAPI-composite solar cells: a) current-voltage characteristics and b) incident photon to current conversion efficiency (IPCE) spectra and the integrated current density. Schematic of the device architecture (inset).

Perovskite	FF (%)	V_{OC} (V)	J_{SC} (mA/cm^2)	PCE (%)
MAPI	76,0 (77±4)	1.09 (1.08±0.02)	21.4 (20±1)	17.7 (17±2)
MAPI-composite	78,1 (72±6)	1.10 (1.08±0.02)	20.0 (19±1)	17.2 (15±3)

Table 1. Solar cell parameters extracted from the best pixels for the MAPI and MAPI-composite. Average values are reported in brackets.

In order to understand how the polymer influences the electronic and ionic properties of the PSCs active layer, we performed a comprehensive study including space charge limited current, thermally stimulated currents, and impedance spectroscopy measurements, respectively.

3.2 Characterization of hole- and electron-only devices by SCLC

SCLC measurements are a relatively simple and powerful method to determine charge carrier mobilities and trap density in the so-called hole-only and electron-only devices [12]. It has been widely used to study steady state charge transport properties in organic semiconductors and also in perovskites. Recently, it has been reported that the classical numerical model, characterized by low permittivity without ion dynamics, is not strictly applicable to SCLC characteristics in perovskites [13],[9]. A more complex numerical model, which considers a mixed ionic and electronic conduction, definitely leads to better fit of the entire J-V characteristics and it allows a better understanding of the physical phenomena governing this new class of materials [13]. While keeping this in mind, analytical equations remain a powerful tool to fit the experimental data in a narrow range of the J-V characteristics, such as the "trap-free regime", allowing us to estimate charge carriers mobility.

Hole mobility measurements were performed on unipolar devices having the following structure: ITO/PEDOT/Perovskite/MoO_3/Au. Fig. 3a shows a schematic of the energy levels for the hole-only devices.

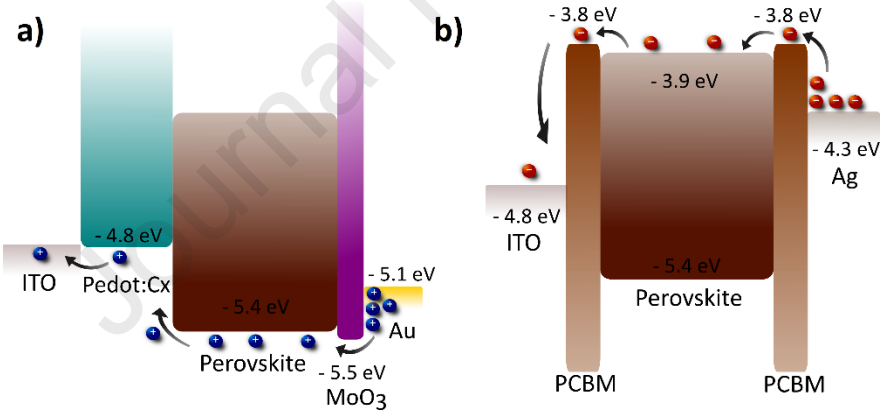

Figure 3. Schematic of the energy levels of the (a) hole-only and (b) electron-only devices realized for the SCLC measurements.

In the case of MAPI-based devices, we clearly identify four regimes (see Fig. 4a) with each one characterized by a different power-low voltage dependence on the current ($J \propto V^n$). At low voltages, the current is proportional to the applied bias in the so-called ohmic regime (n = 1), which reflects the presence of good ohmic contacts and where the current derives from the equilibrium charges. As the external bias is increased, we enter into the so-called space charge regime where the injected charge density exceeds the intrinsic free carrier density and the current is bulk limited. We identify three space charge limited current regimes: i) trap-limited SCLC (TL-SCLC), where the current is proportional to the square of the applied voltage (n = 2) typical of a "pure" space charge regime (however, its amplitude is much lower due to the presence of traps which limit the current

flow); ii) as we increase the external bias further, the density of free carriers starts to exceed the trapped ones and we have the so-called trap-filling regime (TFL-SCLC, n > 3); iii) finally, once all the traps have been filled, all the injected charges participate in the current flow and give rise to trap-free charge transport (TF-SCLC) where the current-voltage characteristic is described by the well-known Mott-Gurney relation (n = 2) [14]:

$$J = \frac{9}{8}\mu\varepsilon_r\varepsilon_0\frac{V^2}{L^3} \quad (1)$$

where V is the external applied voltage, μ is the "trap-free" mobility, ε_0 the vacuum permittivity, ε_r the relative permittivity, and L is the sample thickness. This latter regime allowed us to determine the mobility values by fitting the current-voltage characteristics according to Eq. (1) (see Fig. S5). The average hole mobility, estimated from several nominal identical devices, was found to be (1.1±0.3) x 10^{-3} cm^2/Vs for MAPI, which is in good agreement with previously reported results [15],[16]. In similar way, we measured the average hole mobility of the MAPI-composite and it was found to be (1.8±0.8) x 10^{-3} cm^2/Vs. We can clearly see that as we move from a neat perovskite active layer to a MAPI-composite, the charge carrier mobility does not change. This result implies a good optimization of the perovskite-polymer ratio [3], which allows a percolation path between the perovskite sites that gives a hole mobility similar to that of the pristine film. This latter observation can explain the similar performances of MAPI and MAPI-composite solar cells (see Table 1). Furthermore, from the analysis of the current-voltage curves, the TL-SCLC regime is missing in the MAPI-composite sample, which shows a direct transition from the ohmic to the TFL regime. The presence of a broad peak in the slope, between the linear regime and the TFL one, can be ascribed to trap sites [17],[18]. We argue that the polymer could inhibit the formation of these trap sites close to the valence band. The suppression of these traps can occur either during film processing or by hindering the drift of positive ions, leaving fixed negatively-charged ions, which may act as trap states for positive free carriers (holes) [19],[20],[21]. Usually, the TFL regime allows the quantification of the trap density via the so-called V_{TFL}, which is based on a simplified model that assumes a single level of traps [14],[22]. In the present case, anticipating later results (see Section 3.3), we observe a trap distribution. Furthermore, Duijnstee et al. [23] have recently reported that the classical (steady state) SCLC method can lead to a wrong estimation of the charge traps density because of the ionic conductivity. To overcome these issues, in the present paper, we study charge traps density and distribution by TSC, which directly allows the investigation of defect states within the bandgap without any external applied bias, thus reducing any ionic drift.

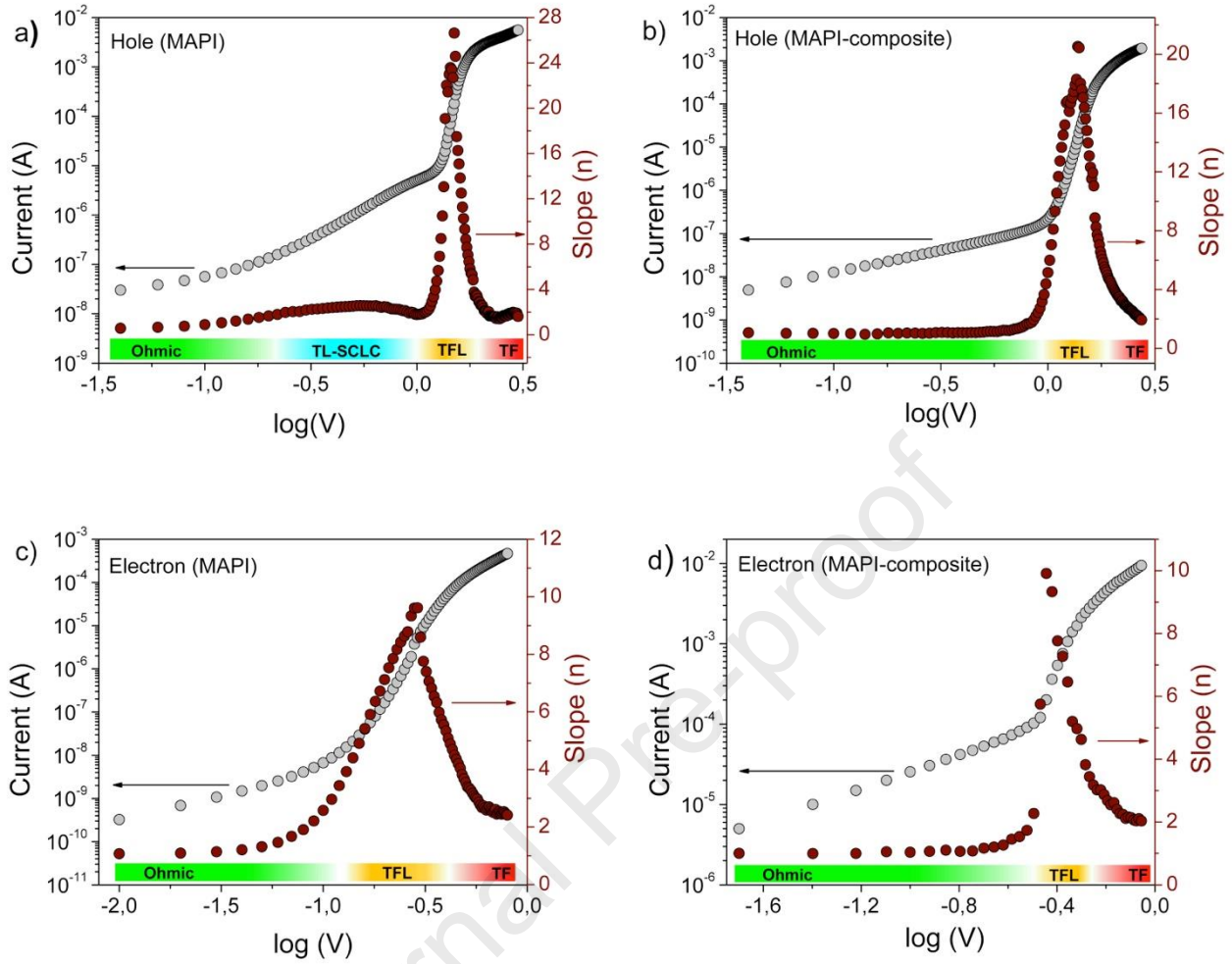

Figure 4. Current- and slope- voltage curves for hole-only and electron-only devices for the (a,c) MAPI and the (b,d) MAPI-composite.

We also measured the electron mobility in electron-only devices with the following layout: ITO/PCBM/Perovskite/PCBM/Ag, as shown in Fig. 3b. We saw from Fig. 4(c, d) that the current-voltage curves are quite similar for electrons, which implies a similar charge transport scenario for electrons in the MAPI and in the MAPI-composite. The average electron mobility was found to be $(1.2 \pm 0.2) \times 10^{-3}$ cm^2/Vs for the MAPI and $(2 \pm 1) \times 10^{-3}$ cm^2/Vs for the MAPI-composite. Also in this case, mobility values are similar between the MAPI and the composite samples. Furthermore, electron mobility values are similar to the hole ones, suggesting an ambipolar charge transport for both materials.

We can conclude that as we move from a neat to a composite perovskite active layer, better device stability (longer lifetime) is not gained at the expense of charge mobility, which is further confirmed by similar device performances.

3.3 Characterization of PSCs by TSC measurements

We investigate the role of the polymer upon traps formation by applying the TSC method to a working solar cell [24],[25],[26],[27]. TSC measurements allow a direct observation of charge traps density and distribution within the bandgap in the absence of any external bias. Thus, ideally, without involving any additional ionic drift.

The $MAPbI_3$ crystal is known to have a phase transition between orthorhombic and tetragonal structures at 162 K [28],[29], thus we first experimentally check the phase transition for both the neat and composite perovskite films by cooling down to 77 K and then warming up to 300 K our devices. Fig. 5 shows the TSC cooling and heating scans performed in the dark, i.e., without any traps filling, which allowed us to safely attribute the peaks to the phase transitions. It has been reported by Baumann and co-workers [25] that dark TSC profiles are polarization currents due to the reversible polarization (depolarization) of the perovskite films during the phase transition from tetragonal to orthorhombic (and vice versa). It is worth noting that our transition peak values are in perfect agreement with the already reported results on MAPI, where a shift of the heating peak between 145 K and 160 K has been observed that was attributed to different scan rates or sample-to-sample variation due to film processing conditions and sample grains [27],[30].

Independently from the absolute value of the MAPI peaks, the MAPI-composite peaks are shifted to higher temperatures likely because of an increased density of defects. According to Dobrovolsky et al. [31], a transition from the tetragonal to orthorhombic phase indeed occurs at higher temperatures when the material is characterized by domains with larger defect concentration.

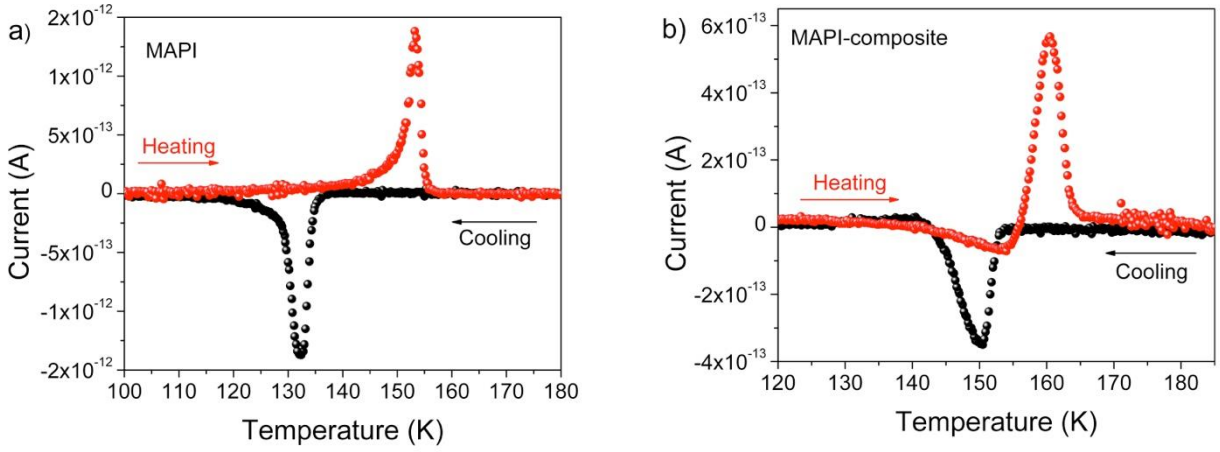

Figure 5. Phase transition for the (a) MAPI and (b) MAPI-composite during cooling and heating in the dark.

Another peculiar characteristic of the MAPI-composite heating scan is the presence of both negative and positive peaks. This means there are contributions from opposite polarization directions that are present within the composite film. It has already been reported that the positive peak contribution in the MAPI perovskite is mainly due to the polarization of the cationic species in the direction perpendicular to the (110) plane [27]. Thus, the additional negative peak seen in our MAPI-composite may be due to a polarization coming from other crystal planes where the cations align in the opposite direction. Indeed, our MAPI thin film has an XRD profile characterized by a main (110) crystallographic orientation (see Fig. S2). Conversely, the MAPI-composite shows a crystallographic orientation characterized by peaks with similar intensities.

Next, we limit the temperature range of our investigation to 160 - 300 K, which means that we remain bound to the tetragonal phase during the entire measurement. This phase is relevant to working PSCs, and also ensures that detected traps are an intrinsic characteristic of the tetragonal phase and not a residual effect from the phase transition. The current resulting from the released carriers as a function of the temperature forms the TSC curves in Fig. 6. The same device structure was used for both materials, and thus the current values can be compared between the two devices. First, the shape of the TSC spectrum indicates a trap distribution instead of a discrete trap level. This is consistent with our SCLC measurements where a gradual rise in the current was seen in the so called TFL regime instead of a steep increase that is typical of a single trap level. By applying Eq. (2) to the TSC scan, we calculate the activation energy of the most prominent traps by

$$E_t = k_B T_{max} ln\left(\frac{T_{max}^4}{\beta}\right), \quad (2)$$

where k_B is the Boltzmann's constant, T_{max} is the temperature at the TSC peak, and β is the heating rate (5 K/min) used in the TSC measurements. The peaks $T_{max,MAPI}$ = 184 K and $T_{max,MAPI\text{-}composite}$ = 190 K correspond to trap depths of 369 meV ($E_{T,MAPI}$) and 384 meV ($E_{T,MAPI\text{-}composite}$), respectively. We can also say that there is a good similarity between the dominant trap states in both samples. A lower limit of the trap density N_t was obtained by integrating the TSC spectrum over time according to Eq. (3) [32]:

$$N_T \geq \frac{1}{ALe\,\beta} \int_{T_i}^{T_f} I(T)\, dT\,, \quad (3)$$

where *I(T)* is the TSC current signal, T_i and T_f are, respectively, the initial and final temperature scan, the integral $\int_{T_i}^{T_f} I(T)\, dT$ is the area under the TSC peak, which is equal to the number of charges

(in this case, holes and electrons) released from the sample during the heating process, *e* is the electronic charge, A is the active device area, and L is the layer thickness.

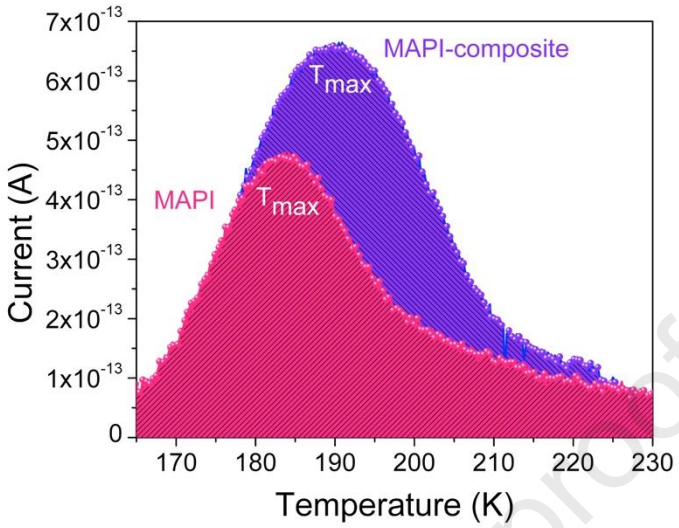

Figure 6. TSC signals for both the MAPI (red curve) and MAPI-composite (blue curve). Both scans have been performed by heating the samples at a scan rate of 5 K/min after optically filling the traps at 160 K.

For pristine MAPI films, we found a trap concentration of $6x10^{14}$ cm^{-3}, which is in very good agreement with the one already reported by TSC measurements for MAPI films [25]. Furthermore, in MAPI-composites, we measured a concentration of $10x10^{14}$ cm^{-3} defects. This difference well explains the observed higher temperature of its phase transition. The larger concentration of defects in the MAPI-composite than that of MAPI could be possibly attributed to its polycrystalline heterogeneity, which is clearly visible in Fig. S3. The MAPI-composite SEM image reveals the presence of well-defined polycrystalline domains whose boundaries may be the source of the larger traps' density seen in our TSC signal. This is a consequence of the polymer-assisted growth of our perovskite-composite film, which, on the one hand, allows a simpler deposition method compared to the standard ones. However, on the other, it does not permit fine control over film formation. Noticeably, our SCLC measurements demonstrated that the increased defect density in the MAPI-composite does not affect the charge carrier mobility. This could be explained by the material's well-known tolerance to defects [33],[34],[35],[36].

3.4 Impedance spectroscopy characterization

Perovskite semiconductors are characterized by a mixed ionic and electronic charge transport mechanism. Thus, to gain insight into the possible influence of the polymer into ion migration, we perform impedance spectroscopy measurements in a temperature range of 250 – 300

K. Fig. S7 shows the Nyquist (Z´-Z´´) plots of impedance spectra for both studied configurations. The Nyquist diagrams for both samples are characterized by a complete and well-defined high-frequency arc and a second low-frequency arc whose definition depends on temperature range. The corresponding Bode plots in Fig. 7 display two peaks: one in the high frequency region and the other in the low frequency region. Analysis of the spectra reveals the existence of two kinetic processes with different time constants at high and low frequencies [37],[38]. It is worth noting that the high frequency signal is independent to temperature variation. In contrary, the low-frequency signal varies accordingly and results in a shift towards higher frequencies when the sample is heated. This finding suggests that in the low frequency region of the spectra, we probed processes such as ionic migrations and/or chemical reactions that are thermally activated, whereas the high frequencies regime is usually attributed to pure electronic processes.

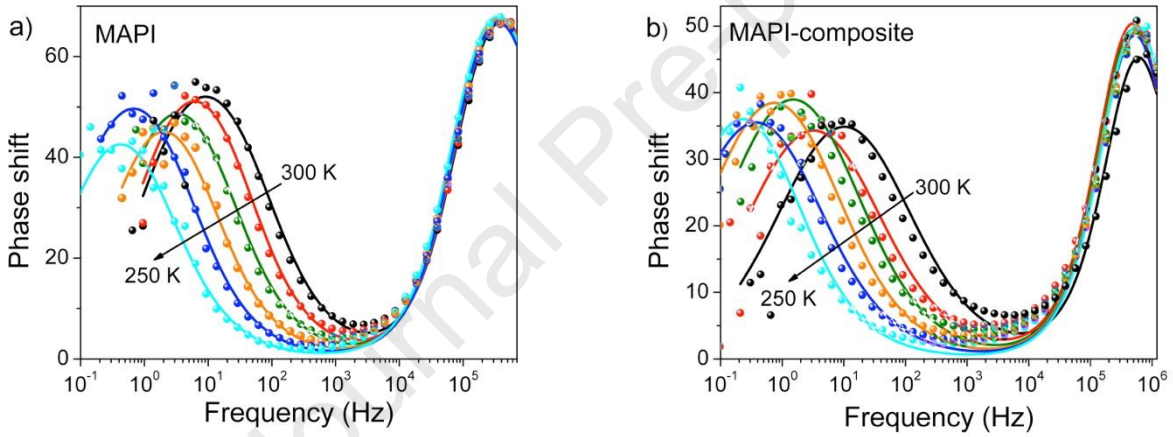

Figure 7. Bode plots of impedance spectra obtained under 1 sun illumination and zero bias for (a) MAPI and (b) MAPI-composite-based devices. Measurements were performed in a temperature range of 250 - 300 K at steps of 10 K. Solid lines represent the fit to the experimental data.

In order to estimate the activation energy for ion migration, Arrhenius plots were elaborated from the low frequency data extracted from Fig. 7. By fitting the impedance spectra at different temperatures with the equivalent circuit shown in Fig. S6 the characteristic time constant of the low frequency component (τ_{LF}) was calculated. The activation energy (E_a) is related to τ_{LF} and to the temperature by the following equation:

$$\frac{1}{\tau_{LF}} = Ae^{-\frac{E_a}{k_B T}} + C, \qquad (4)$$

where *A* is the Arrhenius prefactor, k_B is the Boltzmann constant, T is the temperature, and C is a constant. The variation of the low frequency time constant ($\ln(\tau_{LF}/T)$) with the inverse of the

absolute temperature (1000/T) for MAPI and MAPI-composite based devices is shown in Fig. 8 where the circles are the experimental data and the solid lines are the least-squares straight-line fit.

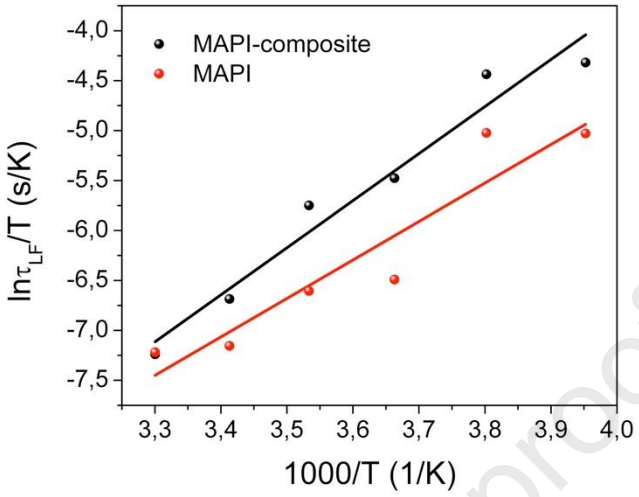

Figure 8. Arrhenius-like plot ln(τ_{LF}/T) versus 1000/T for MAPI and MAPI-composite. The circles are the experimental data and the solid line is the least-squares straight-line fit.

We derived the activation energies from the slopes of the linear fit to the experimental data plotted in Fig. 8, which was about 40 and 31 kJ/mol for MAPI-composite and MAPI, respectively, with the latter one in agreement with previous literature [38],[39],[40]. It looks like the MAPI-composite is characterized by a slightly larger ionic activation energy that translates into a lower ionic conductivity that positively impacts the device stability [3]. Further investigation is ongoing in order to understand the influence of polymers on the ionic activation energy. This important result suggests additional advantages of the composite approach beyond easy processability.

Conclusions

In conclusion, we studied the electronic transport, trapping phenomena, phase transition, and ionic activation energy of pristine and MAPI-starch perovskite films. Our results revealed how the presence of the biopolymer impacts charge traps and ion mobility within the perovskite active layer. We observed that the MAPI-composite still retains its ambipolar charge transport nature and the same mobility values of the MAPI perovskite. This means that as we move from a neat to a composite perovskite active layer, the benefits like improved device stability, mechanical flexibility, and simpler processing are not at the expense of charge transport. Furthermore, the composite showed a lower ionic conductivity that nicely explains the higher stability with respect to the bare

perovskite. These results provide a powerful guideline for the design of novel and better performing perovskite-polymer composites that anticipate the large-scale production of efficient and stable PSCs.

References

[1] NREL efficency, www.nrel.gov/pv/cell-efficiency.html.

[2] D. Li, D. Zhang, K. Lim, Y. Hu, Y. Rong, A. Mei, N. Park, H. Han, A Review on Scaling Up Perovskite Solar Cells, Adv. Funct. Mater. 31 (2021) 2008621. https://doi.org/10.1002/adfm.202008621.

[3] A. Giuri, S. Masi, A. Listorti, G. Gigli, S. Colella, C. Esposito Corcione, A. Rizzo, Polymeric rheology modifier allows single-step coating of perovskite ink for highly efficient and stable solar cells, Nano Energy. 54 (2018) 400–408. https://doi.org/10.1016/j.nanoen.2018.10.039.

[4] T.H. Han, J.W. Lee, C. Choi, S. Tan, C. Lee, Y. Zhao, Z. Dai, N. De Marco, S.J. Lee, S.H. Bae, Y. Yuan, H.M. Lee, Y. Huang, Y. Yang, Perovskite-polymer composite cross-linker approach for highly-stable and efficient perovskite solar cells, Nat. Commun. 10 (2019) 1–10. https://doi.org/10.1038/s41467-019-08455-z.

[5] A. Fakharuddin, M. Seybold, A. Agresti, S. Pescetelli, F. Matteocci, M.I. Haider, S.T. Birkhold, H. Hu, R. Giridharagopal, M. Sultan, I. Mora-Seró, A. Di Carlo, L. Schmidt-Mende, Perovskite-Polymer Blends Influencing Microstructures, Nonradiative Recombination Pathways, and Photovoltaic Performance of Perovskite Solar Cells, ACS Appl. Mater. Interfaces. 10 (2018) 42542–42551. https://doi.org/10.1021/acsami.8b18200.

[6] Z. Safari, M.B. Zarandi, A. Giuri, F. Bisconti, S. Carallo, A. Listorti, C.E. Corcione, M.R. Nateghi, A. Rizzo, S. Colella, Optimizing the interface between hole transporting material and nanocomposite for highly efficient perovskite solar cells, Nanomaterials. 9 (2019). https://doi.org/10.3390/nano9111627.

[7] A. Giuri, Z. Yuan, Y. Miao, J. Wang, F. Gao, N. Sestu, M. Saba, G. Bongiovanni, S. Colella, C. Esposito Corcione, G. Gigli, A. Listorti, A. Rizzo, Ultra-Bright Near-Infrared Perovskite Light-Emitting Diodes with Reduced Efficiency Roll-off, Sci. Rep. 8 (2018) 1–8. https://doi.org/10.1038/s41598-018-33729-9.

[8] S. Gambino, The impact of charge carrier relaxation, electron trapping and oxygen p-doping on the photocurrent transients of a conjugated polymer probed by the Time of Flight method, Thin Solid Films. 718 (2021) 138485. https://doi.org/10.1016/j.tsf.2020.138485.

[9] P. Calado, A.M. Telford, D. Bryant, X. Li, J. Nelson, B.C. O'regan, P.R.F. Barnes, Evidence for ion migration in hybrid perovskite solar cells with minimal hysteresis, Nat. Commun. 7 (2016). https://doi.org/10.1038/ncomms13831.

[10] D. Li, H. Wu, H.C. Cheng, G. Wang, Y. Huang, X. Duan, Electronic and Ionic Transport Dynamics in Organolead Halide Perovskites, ACS Nano. 10 (2016) 6933–6941. https://doi.org/10.1021/acsnano.6b02795.

[11] P. Lopez-Varo, J.A. Jiménez-Tejada, M. García-Rosell, S. Ravishankar, G. Garcia-Belmonte, J. Bisquert, O. Almora, Device Physics of Hybrid Perovskite Solar cells: Theory and Experiment, Adv. Energy Mater. 8 (2018). https://doi.org/10.1002/aenm.201702772.

[12] M. Kuik, G.-J.J.A.H. Wetzelaer, H.T. Nicolai, N.I. Craciun, D.M. De Leeuw, P.W.M. Blom, 25th anniversary article: Charge transport and recombination in polymer light-emitting diodes, Adv. Mater. 26 (2014) 512–531. https://doi.org/10.1002/adma.201303393.

[13] M. Sajedi Alvar, P.W.M. Blom, G.-J.A.H. Wetzelaer, Space-charge-limited electron and hole currents in hybrid organic-inorganic perovskites, Nat. Commun. 11 (2020) 4023. https://doi.org/10.1038/s41467-020-17868-0.

[14] K.C. Kao, Dielectric Phenomena in Solids, Elsevier, 2004.

[15] Y. Chen, J. Peng, D. Su, X. Chen, Z. Liang, Efficient and balanced charge transport revealed in planar perovskite solar cells, ACS Appl. Mater. Interfaces. 7 (2015) 4471–4475. https://doi.org/10.1021/acsami.5b00077.

[16] J. Peng, Y. Chen, K. Zheng, T. Pullerits, Z. Liang, Insights into charge carrier dynamics in organo-metal halide perovskites: From neat films to solar cells, Chem. Soc. Rev. 46 (2017) 5714–5729.

https://doi.org/10.1039/c6cs00942e.

[17] G. Zuo, Z. Li, O. Andersson, H. Abdalla, E. Wang, M. Kemerink, Molecular Doping and Trap Filling in Organic Semiconductor Host-Guest Systems, J. Phys. Chem. C. 121 (2017) 7767–7775. https://doi.org/10.1021/acs.jpcc.7b01758.

[18] G. Zuo, M. Linares, T. Upreti, M. Kemerink, General rule for the energy of water-induced traps in organic semiconductors, Nat. Mater. 18 (2019) 588–593. https://doi.org/10.1038/s41563-019-0347-y.

[19] M. De Bastiani, G. Dell'Erba, M. Gandini, V. D'Innocenzo, S. Neutzner, A.R.S. Kandada, G. Grancini, M. Binda, M. Prato, J.M. Ball, M. Caironi, A. Petrozza, Ion migration and the role of preconditioning cycles in the stabilization of the J-V characteristics of inverted hybrid perovskite solar cells, Adv. Energy Mater. 6 (2016) 1–9. https://doi.org/10.1002/aenm.201501453.

[20] Z. Xu, T. De Rosia, K. Weeks, Photoluminescence-voltage (PL-V) hysteresis of perovskite solar cells, J. Phys. Chem. C. 121 (2017). https://doi.org/10.1021/acs.jpcc.7b06711.

[21] M. Sajedi Alvar, P.W.M. Blom, G.A.H. Wetzelaer, Device Model for Methylammonium Lead Iodide Perovskite With Experimentally Validated Ion Dynamics, Adv. Electron. Mater. 6 (2020) 1900935. https://doi.org/10.1002/aelm.201900935.

[22] S. Chaudhary, S.K. Gupta, C.M. Singh Negi, Enhanced performance of perovskite photodetectors fabricated by two-step spin coating approach, Mater. Sci. Semicond. Process. 109 (2020) 104916. https://doi.org/10.1016/j.mssp.2020.104916.

[23] E.A. Duijnstee, J.M. Ball, V.M. Le Corre, L.J.A. Koster, H.J. Snaith, J. Lim, Toward Understanding Space-Charge Limited Current Measurements on Metal Halide Perovskites, ACS Energy Lett. 5 (2020) 376–384. https://doi.org/10.1021/acsenergylett.9b02720.

[24] C. Qin, T. Matsushima, T. Fujihara, W.J. Potscavage, C. Adachi, Degradation Mechanisms of Solution-Processed Planar Perovskite Solar Cells: Thermally Stimulated Current Measurement for Analysis of Carrier Traps, Adv. Mater. 28 (2016) 466–471. https://doi.org/10.1002/adma.201502610.

[25] A. Baumann, S. Väth, P. Rieder, M.C. Heiber, K. Tvingstedt, V. Dyakonov, Identification of Trap States in Perovskite Solar Cells, J. Phys. Chem. Lett. 6 (2015) 2350–2354. https://doi.org/10.1021/acs.jpclett.5b00953.

[26] G. Gordillo, C.A. Otálora, M.A. Reinoso, Trap center study in hybrid organic-inorganic perovskite using thermally stimulated current (TSC) analysis, J. Appl. Phys. 122 (2017) 75304. https://doi.org/10.1063/1.4999297.

[27] S.T. Birkhold, H. Hu, P.T. Höger, K.K. Wong, P. Rieder, A. Baumann, L. Schmidt-Mende, Mechanism and Impact of Cation Polarization in Methylammonium Lead Iodide, J. Phys. Chem. C. 122 (2018) 12140–12147. https://doi.org/10.1021/acs.jpcc.8b00631.

[28] A. Poglitsch, D. Weber, Dynamic disorder in methylammoniumtrihalogenoplumbates (II) observed by millimeter-wave spectroscopy, J. Chem. Phys. 87 (1987) 6373. https://doi.org/10.1063/1.453467.

[29] N. Onoda-Yamamuro, T. Matsuo, H. Suga, Dielectric study of CH3NH3PbX3 (X = Cl, Br, I), J. Phys. Chem. Solids. 53 (1992) 935–939. https://doi.org/10.1016/0022-3697(92)90121-S.

[30] A. Osherov, E.M. Hutter, K. Galkowski, R. Brenes, D.K. Maude, R.J. Nicholas, P. Plochocka, V. Bulović, T.J. Savenije, S.D. Stranks, The Impact of Phase Retention on the Structural and Optoelectronic Properties of Metal Halide Perovskites, Adv. Mater. 28 (2016) 10757–10763. https://doi.org/10.1002/adma.201604019.

[31] A. Dobrovolsky, A. Merdasa, E.L. Unger, A. Yartsev, I.G. Scheblykin, Defect-induced local variation of crystal phase transition temperature in metal-halide perovskites, Nat. Commun. 8 (2017) 34. https://doi.org/10.1038/s41467-017-00058-w.

[32] P. Stallinga, Electrical Characterization of Organic Electronic Materials and Devices, 2009. https://doi.org/10.1002/9780470750162.

[33] A. Zakutayev, C.M. Caskey, A.N. Fioretti, D.S. Ginley, J. Vidal, V. Stevanovic, E. Tea, S. Lany, Defect tolerant semiconductors for solar energy conversion, J. Phys. Chem. Lett. 5 (2014) 1117–1125. https://doi.org/10.1021/jz5001787.

[34] J. Kim, S.-H. Lee, J.H. Lee, K.-H. Hong, The Role of Intrinsic Defects in Methylammonium Lead Iodide Perovskite, J. Phys. Chem. Lett. 5 (2014) 1312–1317. https://doi.org/10.1021/jz500370k.

[35] H. Jin, E. Debroye, M. Keshavarz, I.G. Scheblykin, M.B.J. Roeffaers, J. Hofkens, J.A. Steele, It's a trap! on the nature of localised states and charge trapping in lead halide perovskites, Mater. Horizons. 7 (2020) 397–410. https://doi.org/10.1039/c9mh00500e.

[36] R.E. Brandt, J.R. Poindexter, P. Gorai, R.C. Kurchin, R.L.Z. Hoye, L. Nienhaus, M.W.B. Wilson, J.A. Polizzotti, R. Sereika, R. Žaltauskas, L.C. Lee, J.L. Macmanus-Driscoll, M. Bawendi, V. Stevanović, T. Buonassisi, Searching for "defect-Tolerant" Photovoltaic Materials: Combined Theoretical and Experimental Screening, Chem. Mater. 29 (2017) 4667–4674. https://doi.org/10.1021/acs.chemmater.6b05496.

[37] J.R.M. Barsoukov, Evgenij, Impedance Spectroscopy Theory, Experiment, and Applications, second, John Wiley & Sons, 2005.

[38] L. Contreras-Bernal, S. Ramos-Terrón, A. Riquelme, P.P. Boix, J. Idígoras, I. Mora-Seró, J.A. Anta, Impedance analysis of perovskite solar cells: A case study, J. Mater. Chem. A. 7 (2019) 12191–12200. https://doi.org/10.1039/c9ta02808k.

[39] Y. Yuan, J. Chae, Y. Shao, Q. Wang, Z. Xiao, A. Centrone, J. Huang, Photovoltaic Switching Mechanism in Lateral Structure Hybrid Perovskite Solar Cells, Adv. Energy Mater. 5 (2015) 1–7. https://doi.org/10.1002/aenm.201500615.

[40] S. Meloni, T. Moehl, W. Tress, M. Franckeviius, M. Saliba, Y.H. Lee, P. Gao, M.K. Nazeeruddin, S.M. Zakeeruddin, U. Rothlisberger, M. Graetzel, Ionic polarization-induced current-voltage hysteresis in CH3NH3PbX3 perovskite solar cells, Nat. Commun. 7 (2016). https://doi.org/10.1038/ncomms10334.

Appendix - Supplementary data

Preparation of MAPI and MAPI-composite solution

The MAPI-composite solution was prepared, according to the method previously developed [1], by solubilizing an equimolar stoichiometry of perovskite precursors, i.e. MAI:PbI_2 = 1:1, in DMSO (precursor concentrations of 30 wt%), at 80 °C for 30 min. After precursors solubilization, 10 wt% starch (respect to perovskite precursors) was added and then stirred at 80 °C for 5 h. The standard MAPI solution was prepared according to literature [2], by solubilizing an equimolar stoichiometry, i.e. MAI:PbI_2:DMSO = 1:1:1, in DMF (precursors concentration 48 wt%). All the solutions were prepared inside an N_2 filled glove-box.

MAPI and MAPI-composite thin films characterization

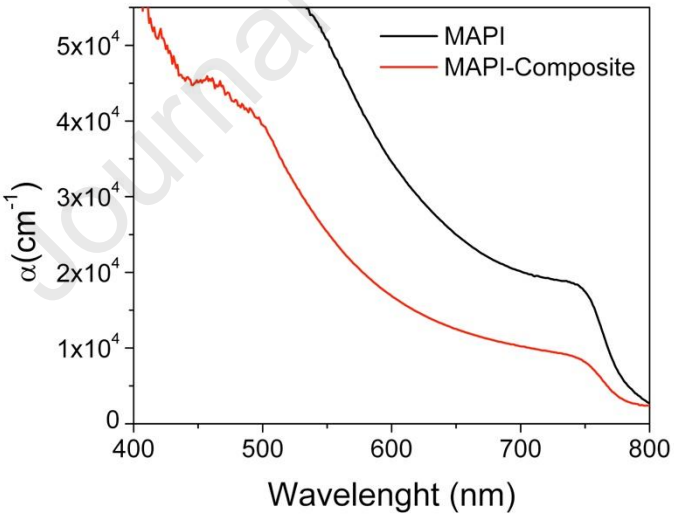

Figure S1. MAPI (black line) and MAPI-composite (red line) thin film absorption coefficient in the visible range.

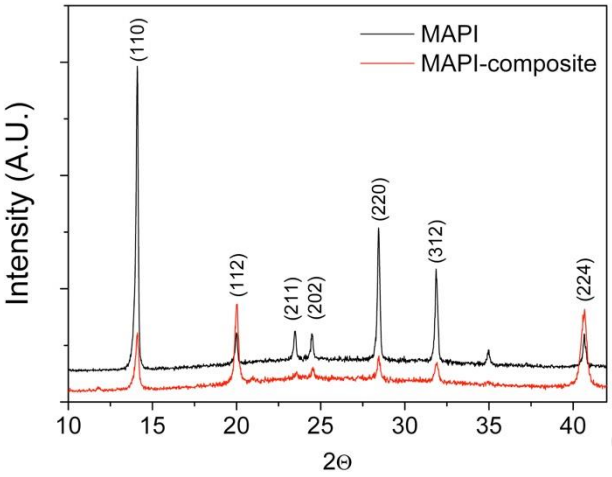

Figure S2. XRD spectra acquired on MAPI (black line) and MAPI-composite (red line) thin films.

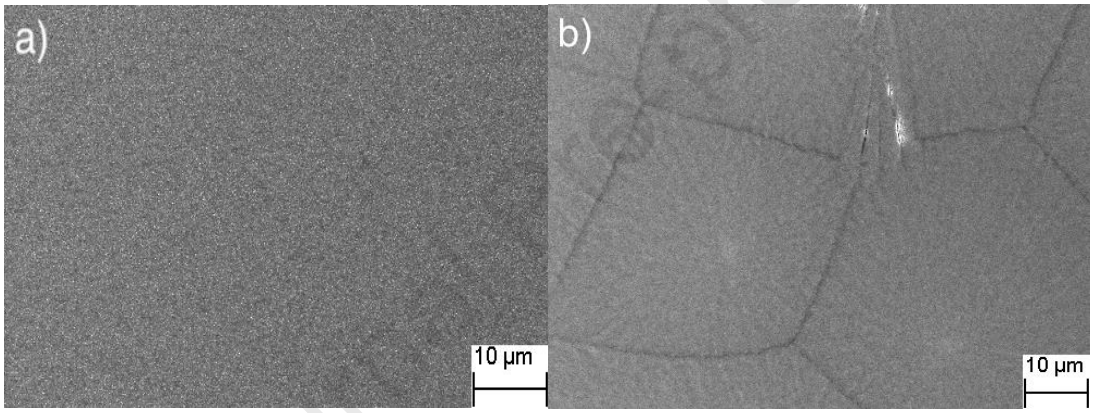

Figure S3. SEM images of (a) MAPI and (b) MAPI-composite thin films.

Solar Cells Realization and Characterization

p-i-n solar cells were realized as follow: glass/ITO/poly-TPD/perovskite/ PCBM/BCP/Ag. ITO coated glass substrates were cleaned by ultrasonication in acetone and 2-propanol, and then underwent to an oxygen plasma treatment. Poly-TPD (1.5 mg/ml in chlorobenzene) was deposited on top of ITO by spin coating at 4000 rpm for 60 s, and annealed at 110 °C for 30 min in air. The resulting film was then exposed to UV light in air (30 min) to improve its surface wettability. Subsequently, the MAPI or MAPI-composite was spin coated, as described in Section 2.2, on top of poly-TPD. PCBM (25 mg/ml in chlorobenzene) and BCP (0.5 mg/ml in isopropanol) solutions were sequentially deposited onto the active layer at 6000 rpm for 60 s and 5000 rpm for 20 s, respectively. Finally, a thin film of silver (Ag) was deposited through a shadow mask by high vacuum thermal evaporation, defining an active area of about 0.04 cm^2. However, in order to minimize any error due

to sample-to-sample variation and to make our device efficiency calculations more reliable, we measured "the real" active area of each single device using an optical microscope (Olympus BX51).

Solar cells were characterized in N_2 atmosphere, under standard conditions of light intensity (100 mW/cm^2, AM1.5) using a solar simulator (Newport 91160A) and a source measure unit (Keithely 2400). Devices current-voltage characteristics were acquired in a voltage range of -0.2 ÷ 1.2 V. The IPCE was measured in air using a power source (Newport xenon lamp, 140 W, 67005) coupled with a monochromator (Newport Cornerstore 260 Oriel 74125), a photodiode (Newport Oriel 71675_71580) and a dual channel optical power/energy meter (Newport 2936-C).

Fabrication and characterization of electron-only and hole-only devices

Unipolar devices were realized in order to perform SCLC measurements. Hole-only devices, were realized as follow: ITO/PEDOT:Cx/Perovskite/MoO_3/Au. Pedot:Cx was spin coated at 8000 rpm for 60 s and was annealed at 140°C for 15 min in air. Pedot-complex (Pedot:Cx) was used instead of Pedot:PSS, because DMSO dissolves the latter one [3,4]. Then, the perovskite active layer was deposited as reported in Section 2.2. Finally, a thin film of MoO_3 (10 nm) and Au (50 nm) were deposited through a shadow mask by high vacuum thermal evaporation. Electron-only devices were realized as follow: ITO /PCBM/Perovskite/PCBM/Ag. The bottom PCBM layer (10 mg/ml in chlorobenzene) was spin coated on top of ITO at 2000 rpm for 30 s, and then annealed at 100 °C for 10 min inside a glove-box. The top PCBM layer (25 mg/ml in chlorobenzene) was spin coated at 1000 rpm for 60 s. Finally, a silver (Ag) cathode (60 nm) completed the device.

Our SCLC measurements are shown in the main text both in the form of current-voltage and slope-voltage characteristics. The slope (n) is defined as follow:

$$n = \frac{dlogJ}{dlogV}$$

Usually, the slope-voltage curves are important as their peak position and height give us important information about charge trap density and depth, respectively [5]. While the current-voltage curve gives basically information about the magnitude of the charge carrier mobilities. The slope represents the power law dependency of the current density on the applied voltage $J \propto V^n$. Thus, we can associate the different values of *n* to different space charge limited regimes, as shown in Fig. S4.

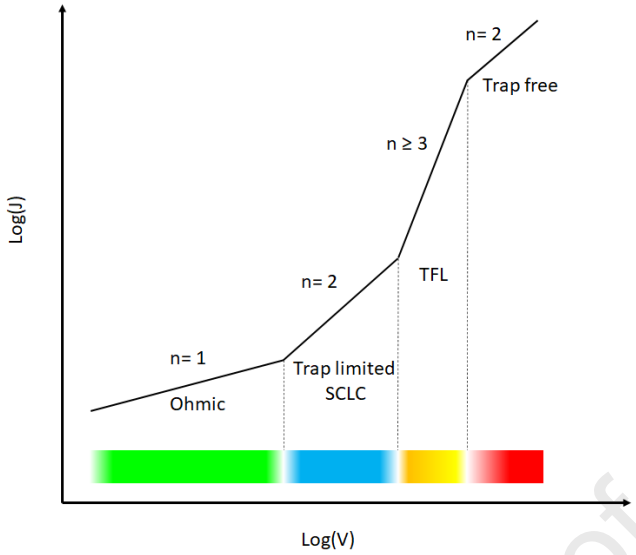

Figure S4. Schematic of an ideal SCLC characteristic on log-log scale. According to the *n* value we identified four regions: i) Ohmic regime, ii) trap-limited SCLC, iii) trap filling SCLC and iv) trap-free SCLC.

In order to estimate the hole and electron mobility values, we fitted the trap-free regime of the current-voltage characteristic according to Eq. 1 (see Section 3.2) and assuming a constant (high frequency) value of the dielectric permittivity (ε_r = 24) [6].

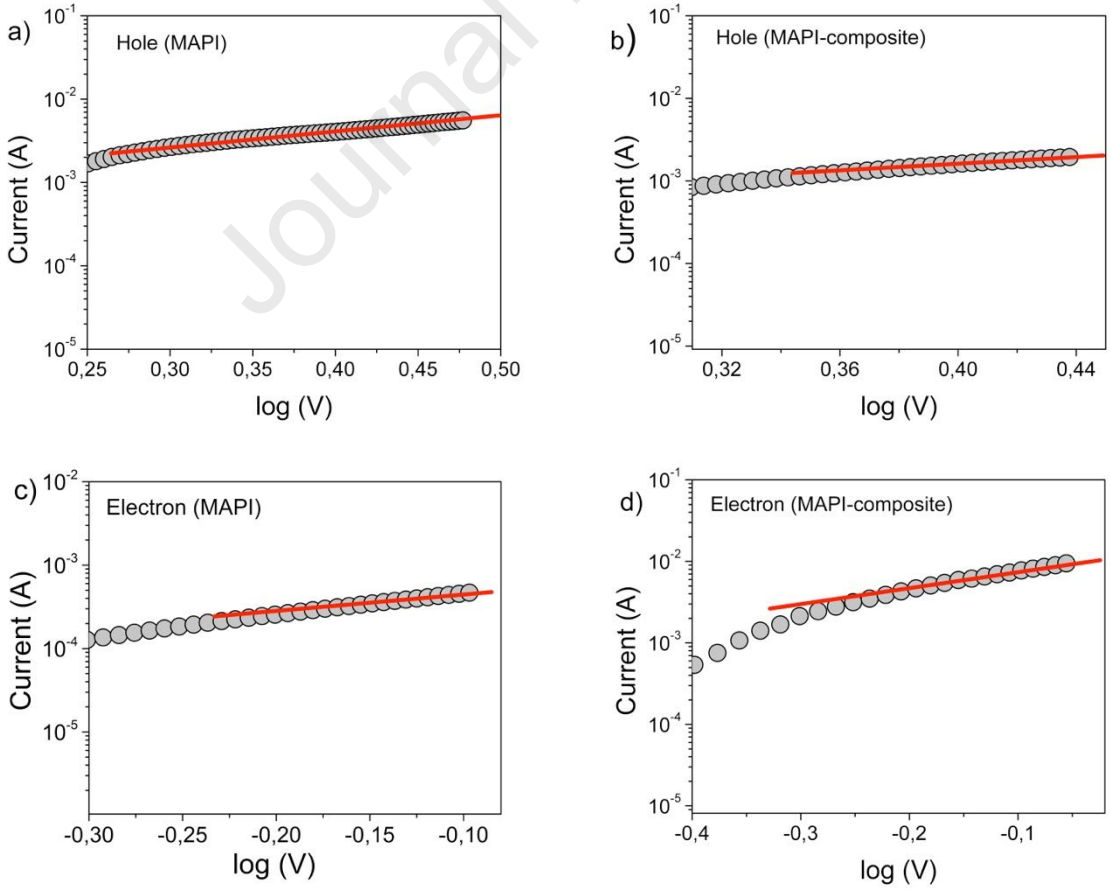

Figure S5. Current-voltage data (grey circles) of the (a, b) hole-only and (c, d) electron-only MAPI and MAPI-composite based devices. Solid lines represent the fit to the experimental data according to Mott-Gurney relation (see Eq. 1 in the main text) in the trap-free regime.

IS characterization

The most widely used approaches to fit the experimental data from solar cells are equivalent circuit modeling. It comes from the solution to the continuity equation. However, due to the complex nature of the physical processes involved in PSCs, including mixed electronic-ionic conductivity of perovskite, the equations underlaying this process are not universally accepted [7]. As a consequence, there is not a clear consensus on the selection of the equivalent circuit and on the physical interpretation of the constituent elements [8,9]. Indeed, selecting the appropriate equivalent circuit is not an easy task. Nevertheless, here we adopted a simplified equivalent circuit showed in Fig. S6, in which R_S takes into account the series resistance induced by the electrical ohmic contacts, the capacitance (C HF) and resistance (R HF) describe the phenomena relate to the high-frequency region usually related to the geometrical capacitance and recombination resistance [10]. About the origin of the low frequency region, as discussed in the main text, there is not clear consensus on the physical interpretation, but is widely accepted that ionic movement is related to the origin of this feature.

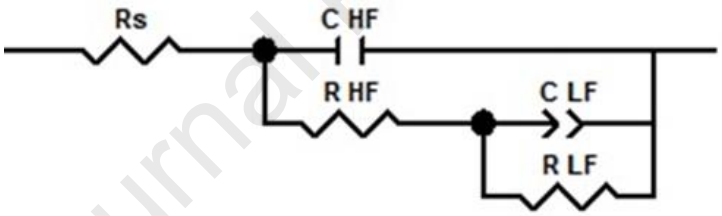

Figure S6. Equivalent circuit used to fit the IS spectra of the MAPI and MAPI-composite based solar cell.

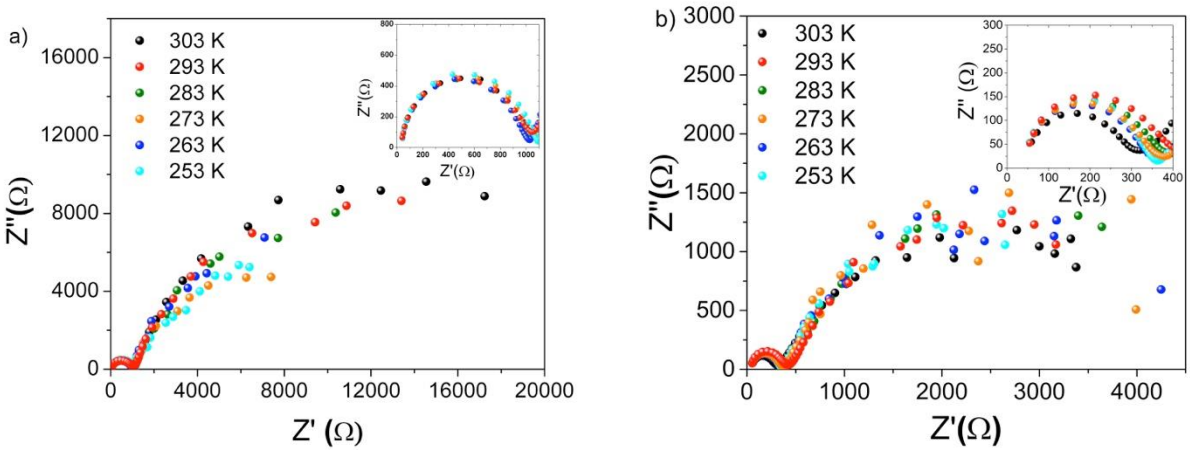

Figure S7. Nyquist plot of the impedance spectroscopy carried out in the 253-303 K temperature range for a) MAPI and b) MAPI-composite.

References

[1] A. Giuri, S. Masi, A. Listorti, G. Gigli, S. Colella, C. Esposito Corcione, A. Rizzo, Polymeric rheology modifier allows single-step coating of perovskite ink for highly efficient and stable solar cells, Nano Energy. 54 (2018) 400–408. https://doi.org/10.1016/j.nanoen.2018.10.039.

[2] N. Ahn, D.Y. Son, I.H. Jang, S.M. Kang, M. Choi, N.G. Park, Highly Reproducible Perovskite Solar Cells with Average Efficiency of 18.3% and Best Efficiency of 19.7% Fabricated via Lewis Base Adduct of Lead(II) Iodide, J. Am. Chem. Soc. 137 (2015) 8696–8699. https://doi.org/10.1021/jacs.5b04930.

[3] I. Lee, G.W. Kim, M. Yang, T.S. Kim, Simultaneously Enhancing the Cohesion and Electrical Conductivity of PEDOT:PSS Conductive Polymer Films using DMSO Additives, ACS Appl. Mater. Interfaces. 8 (2016) 302–310. https://doi.org/10.1021/acsami.5b08753.

[4] L. V. Lingstedt, M. Ghittorelli, H. Lu, D.A. Koutsouras, T. Marszalek, F. Torricelli, N.I. Crăciun, P. Gkoupidenis, P.W.M. Blom, Effect of DMSO Solvent Treatments on the Performance of PEDOT:PSS Based Organic Electrochemical Transistors, Adv. Electron. Mater. 5 (2019) 1–8. https://doi.org/10.1002/aelm.201800804.

[5] K.C. Kao, Dielectric Phenomena in Solids, Elsevier, 2004.

[6] N. Onoda-Yamamuro, T. Matsuo, H. Suga, Dielectric study of CH3NH3PbX3 (X = Cl, Br, I), J. Phys. Chem. Solids. 53 (1992) 935–939. https://doi.org/10.1016/0022-3697(92)90121-S.

[7] L. Contreras-Bernal, S. Ramos-Terrón, A. Riquelme, P.P. Boix, J. Idígoras, I. Mora-Seró, J.A. Anta, Impedance analysis of perovskite solar cells: A case study, J. Mater. Chem. A. 7 (2019) 12191–12200. https://doi.org/10.1039/c9ta02808k.

[8] E. Von Hauff, Impedance Spectroscopy for Emerging Photovoltaics, J. Phys. Chem. C. 123 (2019) 11329–11346. https://doi.org/10.1021/acs.jpcc.9b00892.

[9] A. Todinova, L. Contreras-Bernal, M. Salado, S. Ahmad, N. Morillo, J. Idígoras, J.J.A. Anta, Towards a Universal Approach for the Analysis of Impedance Spectra of Perovskite Solar Cells: Equivalent Circuits and Empirical Analysis, ChemElectroChem. 4 (2017) 2891–2901. https://doi.org/10.1002/celc.201700498.

[10] L. Contreras-Bernal, M. Salado, A. Todinova, L. Calio, S. Ahmad, J. Idígoras, J.A. Anta, Origin and Whereabouts of Recombination in Perovskite Solar Cells, J. Phys. Chem. C. 121 (2017) 9705–9713. https://doi.org/10.1021/acs.jpcc.7b01206.

Declaration of interests

☒ The authors declare that they have no known competing financial interests or personal relationships that could have appeared to influence the work reported in this paper.

☐The authors declare the following financial interests/personal relationships which may be considered as potential competing interests: